

https://dspace.org/

# Mossbauer Effect Spectroscopy Of Iron Near The Curie Temperature

**Bleloch, Andrew Luke**

**2015-01-09**
http://hdl.handle.net/10539/16303

Downloaded from a DSpace repository. https://dspace.org/

# MÖSSBAUER EFFECT SPECTROSCOPY OF IRON NEAR THE CURIE TEMPERATURE

Andrew Luke Bleloch

A Dissertation Submitted To The Faculty Of Science
University Of The Witwatersrand, Johannesburg
For The Degree Of Master Of Science

Johannesburg 1985

DECLARATION

I declare that this dissertation is my own, unaided work. It is being submitted for the degree of Master of Science in the University of the Witwatersrand, Johannesburg. It has not been submitted before for any degree or examination in any other University.

Andrew Luka Bleloch

12 day of May, 1985.

TABLE OF CONTENTS

LIST OF FIGURES . . . . . 2

LIST OF TABLES . . . . . 6

ABSTRACT . . . . . 7

INTRODUCTION . . . . . 8

THEORETICAL BACKGROUND . . . . . 11

THE HIGH TEMPERATURE MÖSSBAUER FACILITY . . . . . 23

DATA ANALYSIS . . . . . 37

THE RECOILLESS FRACTION OF IRON CLOSE TO THE CURIE TEMPERATURE . . . . . 42

THE HYPERFINE FIELD OF IRON NEAR THE CURIE POINT . . . . 54

*DISCUSSION* . . . . . 61

REFERENCES . . . . . 65

APPENDIX A . . . . . 67

ACKNOWLEDGEMENTS . . . . . 71

TABLE OF CONTENTS

LIST OF FIGURES . . . . . 2

LIST OF TABLES . . . . . 6

ABSTRACT . . . . . 7

INTRODUCTION . . . . . 8

THEORETICAL BACKGROUND . . . . . 11

THE HIGH TEMPERATURE MÖSSBAUER FACILITY . . . . . 23

DATA ANALYSIS . . . . . 37

THE RECOILLESS FRACTION OF IRON CLOSE TO THE CURIE TEMPERATURE . . . . . 42

THE HYPERFINE FIELD OF IRON NEAR THE CURIE POINT . . . . 54

DISCUSSION . . . . . 61

REFERENCES . . . . . 65

APPENDIX A . . . . . 67

ACKNOWLEDGEMENTS . . . . . 71

## LIST OF FIGURES


| | | |
|---|---|---|
| Figure 1.1 | Resonant absorption of nuclear γ rays with the experiment illustrated schematically. | 9 |
| Figure 1.2 | The decay scheme of $^{57}Fe$ | 10 |
| Figure 2.1 | The permitted transitions in the decay of $^{57}Fe$. | 19 |
| Figure 3.1 | Schematic of the basic components of a Mössbauer spectrometer. | 24 |
| Figure 3.2 | A room temperature Mössbauer spectrum with a $^{57}Co(Rh)$ source and a 25μ natural iron absorber. | 25 |
| Figure 3.3 | Frame used to support the absorber in front of the detector. | 27 |
| Figure 3.4 | A velocity calibration spectrum | 29 |
| Figure 3.5 | A cross section of the Mössbauer oven | 30 |
| Figure 3.6 | Schematic diagram of the temperature controller circuit. | 31 |

Figure 3.7 The variation of the line width as a function of temperature at the Curie temperature. 33

Figure 3.8 The variation of the applied magnetic field as the probe is moved from the South pole to the North pole of the magnet. 34

Figure 3.9 The spectrometer illustrated to scale. 36

Figure 5.1 Illustration of the change in area as a line splits. 45

Figure 5.2 The spectrum of a black absorber recorded with a $^{57}$Co(Rh) source. 46

Figure 5.3 The experimental arrangement for the black absorber method. 47

Figure 5.4 The recoilless fraction of $^{57}Fe^{*}$ in iron consisting of 100% enriched $^{56}$Fe close to $T_C$. (* indicates the excited state.) 50

Figure 5.5 Spectra with a stainless steel absorber and $^{57}$Co($^{56}$Fe) source close to the Curie temperature. 51

Figure 5.6 Absorption area of a 25μ natural iron foil recorded with a $^{57}$Co(Rh) source at temperatures near the Curie point. 53

Figure 6.1 Spectra of iron in various applied fields 0.75K above the Curie temperature. 56

Figure 6.2 Ratios of the line intensities as a function of applied field at 0.75K above the Curie temperature. 57

Figure 6.3 The hyperfine field as a function of applied field at 0.75K above the Curie temperature. 58

Figure 6.4. Hyperfine fields of iron induced by applied fields of 0.1T and 0.2T for temperatures above $T_C$. 59

Figure 6.5 Hyperfine field of iron at 0.76K below the Curie temperature for various applied fields. 60

Figure A.1 Circuit diagram for liquid nitrogen timer/filler 67

Figure A.2 Circuit diagram of pass counter 69

Figure A.3 20mA current loop to RS-232-C signal converter. 70

LIST OF TABLES

Table 1 $\theta_{-2}^{a}$ and $\varepsilon(-2)$ for $T<T_C$ and $T>T_C$ 62

## ABSTRACT

A high temperature facility for Mössbauer effect (ME) spectroscopy has been established. This facility permits ME spectroscopy to be performed at temperatures up to 1200K with a stability of 0.03K. This stability is attained through careful oven design and a feedback temperature controller. A feature of the facility is the ability to apply a homogenous external magnetic field of up to 0.2T. The data analysis of Mössbauer spectra has been improved so that more accurate values can be extracted from the data and complex spectra can be fitted with confidence. Using this facility, the recoilless fraction of $^{57}$Co in iron has been determined in the vicinity of the Curie temperature ($T_C$). A change in the characteristic temperature $\theta_{-1}^{a}$ at the Curie temperature of (40 ± 15)% has been measured. Further, a line broadening of 12% distinct from instrumental broadening, has been observed in iron over a 50K range above and below the Curie temperature. Iron ME spectra have also been acquired as a function of an applied magnetic field in the region of the Curie temperature. From the saturation value of the hyperfine field, the average magnetic moment per iron atom has been determined to be 0.43±0.02$\mu_B$. Anomalous intensity ratios in ME spectra of iron in small applied fields .75K above $T_C$ were observed.

# INTRODUCTION

Prior to Mössbauer's discovery in 1958, it was generally believed that the resonant absorption by a nucleus of a $\gamma$ ray emitted by another nucleus was impossible to detect because some of the nuclear transition energy in emission would be lost in the recoil of the emitter and, similarly, the absorber would require additional energy to provide the recoil in order to conserve momentum. So it was expected that the $\gamma$ ray energy would not match the transition energy even though the nuclear excited state has a finite width because this width is generally much smaller than the recoil energy. In fact, this argument only holds in a gas. If the nucleus is "anchored" in a solid, there is a probability $f$ that the recoil momentum will be absorbed by the entire lattice and so the recoil energy, which is inversely proportional to the mass of the recoiling body, is effectively zero. The $\gamma$ ray is then emitted with the full transition energy and is capable of exciting another nucleus, also imbedded in a solid and thus resonant absorption of nuclear $\gamma$ rays is possible.

Because of the narrow line width of the recoilless $\gamma$-ray distribution, the effect is extremely sensitive to changes in energy. Typically, the line width is of the order of $10^{-8}$eV while the energy of the recoilless $\gamma$ rays is 10keV and so resonant absorption occurs only if the energies match to within 1 part in $10^{12}$. This small energy range can be scanned by moving the source relative to the absorber with a velocity $v$, typically of the order a few millimetres per second. According to the Doppler effect the energy $E_\gamma$ of the emitted $\gamma$ rays is shifted by an amount $\Delta E/E_\gamma = v/c$, where $c$ is the speed of light. The geometry most commonly used is the transmission geometry illustrated in figure 1.1.

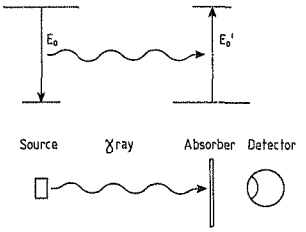


*Fig. 1.1 Resonant absorption of nuclear γ rays with the experiment illustrated schematically.*

$^{57}$Fe was recognised as an important Mössbauer isotope within two years of the discovery of the Mössbauer effect. The decay scheme of this isotope is shown in figure 1.2; it is the 14.41keV transition that is used for Mössbauer effect spectroscopy. There are a number of outstanding questions concerning the Mössbauer effect of pure iron. In particular, in the vicinity of the Curie temperature, there has been relatively little work done. The three major Mössbauer studies at high temperature are those of Preston et al. (1962), Kovats and Walker (1969) and the work of Hohenemser's group (see Kobeissi 1981).

Mössbauer effect studies close to the Curie temperature are of interest because a satisfactory description of the magnetic properties of iron has not yet been developed. That the magnetic moment of iron is not half-integral at room temperature contributed to the development of

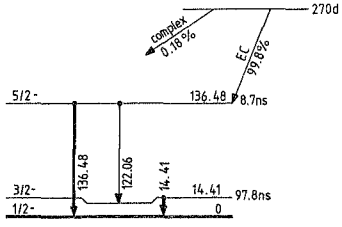


*Fig. 1.2 The decay scheme of $^{57}Fe$.*

itinerant electron models of ferromagnetism, but these models predict a Curie temperature that is an order of magnitude too high (see Hubbard 1978). This has led to the so-called fluctuating band models (see Moriya 1981 for further references). The Mössbauer effect can potentially make a contribution in two areas. Firstly, the recoilless fraction $f$ can be determined; $f$ is related to the mean square displacement of an atom and thus to the phonon distribution. In particular, a change in the recoilless fraction at the Curie temperature would provide information on how the magnetic interaction affects the lattice. Secondly, the hyperfine field is related to the average moment at an atomic site, and so provides a tool for studying the magnetic moment in iron as a function of temperature. To perform such measurements a high-temperature Mössbauer facility had to be built. This facility and measurements performed with it are described in this thesis.

## THEORETICAL BACKGROUND

The various interactions involved in the Mössbauer effect will be introduced by looking at the Hamiltonian of an excited nucleus in a solid. This chapter should provide a background for the results presented in chapters 4 and 5. The emphasis is on the physics behind the formalism rather than on the mathematical intricacies of the formalism.

### Recoilless emission of a gamma ray

The probability that a photon with a wavevector k (and energy $\hbar\omega$) is emitted by a nucleus in a solid is given by,

$$P_{\lambda\alpha}(\mathbf{k}) \propto \frac{|\langle\alpha|\mathcal{H}|\lambda\rangle|^2}{(\hbar\omega+\mathcal{E}_\alpha-\mathcal{E}_\lambda)^2+\frac{1}{4}\Gamma^2_\lambda} \qquad (2.1)$$

where $\mathcal{H}$ is the Hamiltonian describing the nucleus and the solid, and $\lambda$ and $\alpha$ denote the initial and final states of this system, respectively. $\mathcal{E}_\alpha$ and $\mathcal{E}_\lambda$ are the energies corresponding to the states $\alpha$ and $\lambda$. Considered as a function of the photon energy $\hbar\omega$, equation 2.1 has a Lorentzian shape with a full width at half maximum (FWHM) of $\Gamma_\lambda$. This FWHM is related to the meanlife $\tau$ of the state $\lambda$ by the Heisenberg uncertainty relation $\Gamma_\lambda = \hbar/\tau$ .

Equation 2.1 is the familiar result for spontaneous decay from one state to another, a derivation with reference to the Mössbauer effect can be

found in Kolk (1984). The evaluation of the matrix element $\langle\alpha|\mathcal{H}|\lambda\rangle$ and the energy difference $(\mathcal{E}_\alpha - \mathcal{E}_\lambda)$ is the essence of Mössbauer theory.

The first dissection of equation 2.1 is to differentiate between the lattice and the essentially nuclear contributions. To do this, the matrix element $\langle\lambda|\mathcal{H}|\alpha\rangle$ must first be considered in more detail. The nuclear quantum numbers have their usual meaning; i.e. $j$ is the nuclear spin, $m$ is the magnetic quantum number and $\pi$ is the parity. $C$ denotes the quantum numbers of the lattice. The subscripts $g$ and $e$ denote the ground and excited states, respectively.

$$\langle\lambda|\mathcal{H}|\alpha\rangle = \langle\langle j_g m_g \pi_g C_g \ |\mathcal{H}| j_e m_e \pi_e C_e \rangle\rangle_T \qquad (2.2)$$

where $\langle O \rangle_T$ is the thermal average of the operator at temperature T. In the Mössbauer effect, we are only concerned with the probability of recoilless emission. Recoilless implies that the solid does not change state when the $\gamma$ ray is emitted. Therefore, from now on we assume that $C_g = C_e$ (i.e. it does not give energy to or take energy from the $\gamma$ ray).

Having assigned the relevant quantum numbers, the nuclear Hamiltonian for an excited nucleus may be written as

$$\mathcal{H}_n = \frac{-1}{c}\sum_i j(R_i).A(R_i) \qquad (2.3)$$

where $c$ is the speed of light, $j(R_i)$ is the current density of nucleon $i$ and $A(R_i)$ is the vector potential at nucleon $i$. The average position of the nucleus is assumed to be at the origin of our coordinate system, and $R_i = u + r_i$, where u is the position of the centre of mass of the nucleus and $r_i$ is the position of nucleon $i$ with respect to the centre of mass of the nucleus. The vector potential has the form

$$A(R_I) = const \sum_{k,\xi} a^{\dagger}(k,\xi)\ e(k,\xi) exp(-i\ k.r_I) \qquad (2.4)$$

where $a^{\dagger}(k,\xi)$ is a photon creation operator and $e(k,\xi)$ is a unit polarisation vector. If equation 2.4 is substituted in equation 2.3 and one applies the adiabatic approximation, so that the total wave function can be separated into a nuclear and a lattice part, the expression for $\langle\lambda|\mathcal{H}|\alpha\rangle$ reduces to

$$\langle\lambda|\mathcal{H}|\alpha\rangle = \langle J_g m_g \pi_g C_g\ |\mathcal{H}_n|\ J_e m_e \pi_e C_e\rangle \langle\langle G|e^{-i\ k.u(I)}|G\rangle\rangle_T \qquad (2.5)$$

The adiabatic approximation means that no energy transfer takes place between the nucleus and its surroundings. This is usually a good assumption since the surrounding electrons and fields can be considered as static compared to the time scales in the nucleus.

The last factor in equation 2.5 is related to the recoilless fraction. The first factor is the free nucleus transition matrix that determines the relative transition probability amplitudes for the different substates of the nucleus.

Theory of the recoilless fraction

The modulus squared of the lattice part of equation 2.5 is defined as the recoilless fraction,

$$f \equiv |\langle\langle G|e^{-i\ k.u}|G\rangle\rangle_T|^2 \qquad (2.6)$$

which is the probability that no phonons are generated or absorbed when a photon (with wavevector k) is emitted (or absorbed) by a particular nucleus. The thermal average denoted by $\langle O \rangle_T$ is defined by

$$\langle O \rangle_T \equiv \frac{Tr[exp(-\mathcal{H}/k_B T)\ O]}{Tr[exp(-\mathcal{H}/k_B T)]} \qquad (2.7)$$

where $\mathcal{H}$ is the Hamiltonian of the system and $k_B$ is the Boltzman constant. As a notational convenience, $\langle\langle O|O|O\rangle\rangle_T$ is shortened to $\langle O \rangle_T$ .

To write the expression for $f$ in terms of the Debye-Waller factor, it is useful to write the probability amplitude as a series of so-called cumulants (Kolk (1984) and Kendall (1958))

$$\langle e^{-i\ k.u} \rangle_T = exp(\langle -i\ k.u \rangle_T + \tfrac{1}{2}[\langle(-i\ k.u)^2\rangle_T - \langle -ik.u\rangle^2_T] + \ldots) \qquad (2.8)$$

Without a net external force, the terms with $\langle k.u \rangle$ must be zero; so to second order,

$$f^{\frac{1}{2}} = \langle e^{-i\ k.u} \rangle_T = exp(\tfrac{1}{2}[\ \langle(-ik.u)^2\rangle_T]) \qquad (2.9)$$

which can be rewritten as

$$f = e^{-k^2\langle x^2\rangle_T} \qquad (2.10)$$

where $\langle x^2 \rangle_T$ is the projection of the mean square displacement along the direction of k. In fact this expression is correct to fourth order because the third order (and all other odd order) terms are zero in the series expansion in equation 2.8 in the absence of an external force, and,the fourth order terms cancel in the harmonic limit and are very nearly zero in a real lattice.

The value of $f$ can be determined experimentally yielding $\langle x^2 \rangle_T$ which provides information about the phonon distribution and phonon interactions.

Anharmonic effects

Here an outline of the pseudo-harmonic approximation which follows the treatment given by Kolk (1984) is given. The pseudo-harmonic approximation takes account of the shift in phonon energy due to the expansion of the lattice and the anharmonic terms in the Hamiltonian (phonon-phonon interactions) but does not consider the effect of finite phonon lifetimes.

It is useful to consider the frequency moments of phonons. This facilitates the extension of the harmonic approach to the pseudo- and quasi-harmonic approximations. The frequency moments are defined by

$$\omega_n = \frac{1}{3N} \sum_{\kappa,j} \omega_{\kappa,j}^n \qquad (2.11)$$

The phonons of frequency $\omega_{\kappa,j}$ are characterised by their wavevector $\kappa$ and their polarisation index $j$. It may be conceptually helpful to realise that the moments corresponding to $n=1,2$ and $3$ are simply the average phonon frequency, the variance of the phonon distribution, and the skewness of the phonon distribution, respectively. Using the frequency moments, one can define characteristic temperatures $\theta_n$ and frequencies $\omega_n$

$$\theta_n = \frac{\hbar}{k_B}\,\omega_n = \frac{\hbar}{k_B}\,\{\nu_n(n+3)/3\}^{1/n} \qquad (2.12)$$

so that for a Debye phonon spectrum $\theta_n = \theta_D$ for all $n$.

To describe the mean square displacement of an atom in terms of phonon frequency moments, we express the Hamiltonian of the lattice (to fourth order) in phonon creation and annihilation operators. The atomic displacement u has been expressed by Maradudin (1974) in terms of the phonon field operators. The thermal average (equation 2.7) is then calculated explicitly for the atomic displacement. The auto-correlation function in the resulting expression is evaluated using the suitable Green function. The formula for the mean square displacement then turns out to be

$$k^2\langle x^2\rangle_T = \frac{\hbar k^2}{6MN} \sum_{\kappa j} \frac{\coth(\hbar\omega^a_{\kappa j}/2k_BT)}{\omega^a_{\kappa j}} \qquad (2.13)$$

where $M$ is the mass of atom and $N$ is the number of atoms in the solid. The superscript $a$ denotes the anharmonic frequencies that have been shifted because of lattice expansion and phonon-phonon interaction.

$$\omega^a_{\kappa j} = \omega_{\kappa j}(1 - \varepsilon_{\kappa j}T) \qquad (2.14)$$

where $\varepsilon_{\kappa j}$ is the anharmonic parameter. Anharmonic characteristic temperatures can be defined in exactly the same way as their harmonic counterparts, the only difference being that these temperatures are now themselves temperature dependent. To first order in $T$

$$\theta^a_n(T) = \theta_n\{1-\varepsilon_1(n)T + \ldots\} \qquad (2.15)$$

where $\varepsilon_1(n)$ is a weighted average of the anharmonic parameters $\varepsilon_{kj}$

$$\varepsilon_1(n) = \sum_{kj} \varepsilon_{kj} \omega_{kj}^n / \sum_{kj} \omega_{kj}^n \qquad (2.16)$$

The hyperbolic cotangent in equation 2.13 can be expressed as a series, the leading term of which is the inverse of the argument. Taking only the leading term is adequate provided the temperature is sufficiently high, $T > \theta_{-2}^{\theta}/2\pi$ if one notes that the recoil energy $E_R$ can be expressed as

$$E_R = E_\gamma^2/2Mc^2 \qquad (2.17)$$

then the mean square displacement can be written as

$$k^2\langle x^2\rangle_T = \frac{6E_R\, T}{k_B\,(\theta_{-2}^{\theta})^2} \qquad (2.18)$$

Equation 2.18 will be used to fit the recoilless fraction data in chapter 5.

Hyperfine Interactions

Due to interactions between the nucleus and its surroundings (called hyperfine interactions), the energy levels of the nucleus may be shifted or split. Briefly, the important interactions are (for more detail see, for example, Kalk 1984):

- the isomer shift--caused by a difference in the charge density of the surrounding electrons at the nuclei of the source and absorber.

- the magnetic dipole interaction--the nuclear Zeeman splitting caused by the nuclear dipole moment interacting with the magnetic field at the nuclear site.

- the quadrupole interaction--the spin dependent energy split due to the interaction of the nuclear quadrupole moment with the electric field gradient at the nuclear site.

The calculation of the isomer shift is a subject in itself. Here it is treated simply as a fit parameter. As for the quadrupole splitting, each atom in an iron crystal is in a cubic environment. This means that there can be no electric field gradient, and so this interaction does not occur here.

### The magnetic dipole interaction

It is precisely this interaction that we study in iron at the Curie temperature, so it warrants a section on its own. The magnetic moment of a nucleus is related to its spin J by

$$\vec{\mu} = \mu_n g_n J \qquad (2.19)$$

where $\mu_n$ is the nuclear magneton and $g_n$ is the nuclear gyromagnetic ratio. In an applied magnetic field H, the Hamiltonian describing the magnetic perturbation of the nuclear energy levels,

$$\mathcal{H} = -\vec{\mu}.H = -\mu_n g_n J.H \qquad (2.20)$$

has *eigenvalues*

$$E_m = -g\mu Hm/j \qquad (2.21)$$

where, $m$ is the magnetic quantum number and $j$ the eigenvalue of the spin operator. The nuclear Zeeman splitting is shown in figure 2.1 for the 14.41keV transition of an $^{57}$Fe nucleus. The permitted transition energies are limited by the selection rule that $\Delta m=0,\pm1$ to the six lines shown.

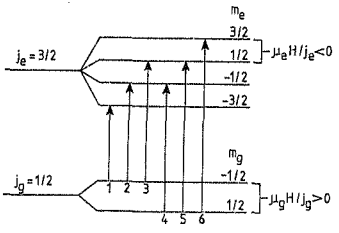


*Fig. 2.1 The permitted transitions in the decay of $^{57}$Fe.*

The origin of the magnetic hyperfine field is manyfold. The various contributions are given by

$$H = H_{applied} + (4/3)\pi M - DM + H_L + H_D + H_S \qquad (2.22)$$

The first three terms are the applied field, the Lorentz field (for cubic symmetry) and the demagnetisation field, respectively. The last three terms are due to the electrons surrounding the nucleus. The fourth term is the contribution from orbital angular momentum, and the fifth is from the dipole field produced at the nucleus by the net spin angular momentum of the electrons. Both these terms are zero in a cubic lattice. The last term is the Fermi contact term and is a result of the difference in density at the nucleus of the two electron spin states. In iron this is the dominant term. Note that only $s$ electrons have a non-zero probability of being at the nucleus. $H_{ns}$ for the $n^{th}$ $s$ electron shell may be written

$$H_{ns} = (8/3)\pi g_e S \mu_B \left(|\psi_{ns\uparrow}(0)|^2 - |\psi_{ns\downarrow}(0)|^2\right) \qquad (2.23)$$

where $\mu_B$ is the Bohr magneton, $g_e$ is the electron gyromagnetic ratio, $S$ is the spin quantum number of the electron ($g_e S = 1$) and $\psi_{ns}(0)$ is the wave function of the $s$ electron with principle quantum number $n$.

The magnitude and sign of the total Fermi contact term are determined by the sum of the polarisations of all the $s$ electron shells. In order to explain the sign of the hyperfine field, the mechanism of core polarisation has to be invoked (Watson and Freeman 1961). Via the exchange interaction, the $s$ electrons are attracted to other electrons of the same spin, say a $d$ electron. If the $d$ electrons have a net spin imbalance, then a polarisation is induced in the $s$ electrons. The sign of this polarisation at the nucleus depends on whether the average radius of the particular $s$ shell is larger than or smaller than the average radius of the $d$ shell. For the innermost $s$ shells, the spin up is attracted outwards by the $d$ electrons producing a spin down at the nuclear site. Conversely, for $s$ electrons with a larger average radius

than the *d* electrons, a spin up is produced at the nucleus. The total *s* electron polarisation at the nuclear site is thus small in comparison with the polarisation of the *s* shells taken individually. In iron the direction of the hyperfine field is opposite to that of the applied magnetic field.

## Transition probabilities

We now consider the free nucleus transition matrix element, $\langle j_g m_g \pi_g | \mathcal{H} | j_e m_e \pi_e \rangle$. The relative probabilities for the different transitions shown in figure 2.1 are given by

$$P(m_g, m_e, \theta) = const \sum_{\xi} |\langle j_g m_g \pi_g | \mathcal{H} | j_e m_e \pi_e \rangle|^2 \qquad (2.24)$$

where $\xi$ is the polarisation of the $\gamma$ ray photon. This equation can be readily deduced from the golden rule. The matrix element can be expressed in terms of a multipole expansion of the vector potential of the radiation field (Rose 1957) with a reduced matrix element, independent of the magnetic substates $m$, as a factor in each term. Including only dipole radiation, the relative probability in equation 2.24 is,

$$P(m_g, m_e, \theta) = \frac{3}{8\pi} \begin{pmatrix} j_g & 1 & j_e \\ m_g & M & -m_e \end{pmatrix}^2 \times \begin{cases} \sin^2\theta & (M=0) \\ \frac{1}{2}(1+\cos^2\theta) & (M=\pm 1) \end{cases} \qquad (2.25)$$

where the matrix is a *3j* symbol defined in Edmonds (1974). Evaluating equation 2.25 for the different transitions gives the familiar 3:2:1:1:2:3 intensity ratio when the quantisation axes are randomly orientated

(demagnetised sample) and the ratio 3:4:1:1:4:3 when all the magnetic hyperfine fields are perpendicular to the incident $\gamma$ rays.

# THE HIGH TEMPERATURE MÖSSBAUER FACILITY

## The Mössbauer Spectrometer

For room temperature measurements, the basic spectrometer illustrated in figure 3.1 was used. The $\gamma$ ray source is attached to one end of the drive motor. The velocity of the source is varied linearly back and forth over a range of about 10mm/s. The $\gamma$ rays are detected, after passing through the absorber, by a proportional counter. The pulses from the proportional counter are amplified and the discriminator is set so that only 14.41keV pulses are counted. These pulses increase the count incrementally in one of the channels of the multi-channel analyser (MCA). The 512 channels are opened one at a time for 400μs each. The start of each sweep through the channels of the MCA is in turn synchronised with the drive motor. The final result is a spectrum of $\gamma$-ray counts as a function of velocity $v$ which is related to the $\gamma$-ray energy $E_\gamma$ through the first order Doppler shift:

$$E_\gamma \approx E_0(1+v/c) \qquad (3.1)$$

where $E_0$ is the energy of the nuclear transition (14.41keV) and $c$ is the speed of light.

At velocities where the energy of the $\gamma$ rays is Doppler shifted so that it corresponds to an excitation energy in the absorber, the $\gamma$ rays are absorbed and a drop in counts is observed. Figure 3.2 shows a spectrum of iron taken at room temperature. The magnetic hyperfine field is responsible for splitting the spectrum into six lines as discussed in chapter 2.

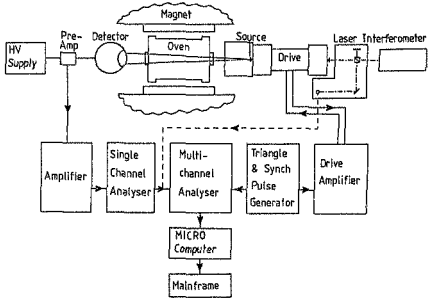


*Fig. 3.1 Schematic of the basic components of a Mössbauer spectrometer.*

One of the sources most commonly used in $^{57}$Fe Mössbauer effect spectroscopy is $^{57}$Co(Rh). The rhodium matrix has the following advantages: it yields a source with a narrow line width (even at high $^{57}$Co concentrations, and low temperatures); and there are no X-rays emitted with energies so close to that of the 14.41keV nuclear $\gamma$ rays that they cannot be resolved by the proportional counter. Two $^{57}$Co sources were used; a weak source of 0.1mCi from the New England Nuclear Corporation (initially 5mCi) and a new strong source of 25mCi from Amersham. The other source used was $^{57}$Co in a pure $^{56}$Fe matrix custom-made by New England Nuclear Corporation. The use of this source will be discussed in chapter 5.

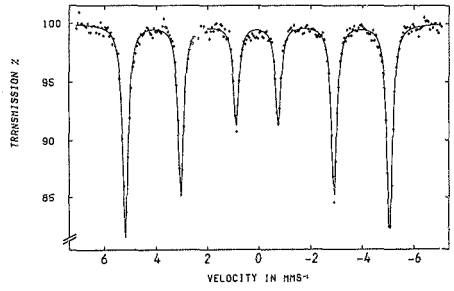


*Fig. 3.2 A room temperature Mössbauer spectrum with a $^{57}Co(Rh)$ source and a 25μ natural iron absorber.*

The proportional counter was filled with a Xe gas of 10% $CO_2$ as the quench gas to a pressure of 2atm. Xe gas at this pressure efficiently absorbs γ rays with energies up to 30keV. This is a useful range for Mössbauer work. The detector window is a 10mil Be foil with a transmission of better than 98% for γ-ray energies above 10keV. A high voltage supply with a stability of 0.5V over 8 hours was set at 2750V. This voltage has proved to be a sensible compromise between detector life and resolution. To reduce the background count, the aluminium casing of the detector was shielded with lead and copper, the former to absorb any high energy radiation that would otherwise penetrate the walls of the detector, and the latter to absorb secondary X-rays produced by the lead. This shielding greatly reduces the background count. In addition, a μ-metal shield was added to exclude the effects of magnetic fields on the detector.

An Austin Science Associates K3 linear motor was used as the drive. The home-built drive amplifier is a second order (2 integrators) feedback loop. This obviates the need for a high gain in the feedback loop to obtain a suitably small error in the motion of the drive and so reduces the tendency for the drive to break into the oscillations associated with high gain feedback systems. The triangular velocity signal for the drive amplifier was produced by a triangle generator. The Nuclear Data MCA we used required an external synchronisation pulse which was also produced by the triangle generator. The positive and negative slopes of the triangle signal were the same to within 5%. Although this is a small difference, it is easily taken into account with the velocity calibration system described below. For most of the spectra the source was mounted on the drive; however, for the series of runs with the source stationary in the oven, a frame was constructed to mount the absorber on the drive. The frame is illustrated in figure 3.3. Some difficulties were experienced in finding suitable materials for constructing the frame. Many of the frames tested caused the system to oscillate at a frequency in the region of 1kHz. The combination of aluminium and balsa wood produced the best results.

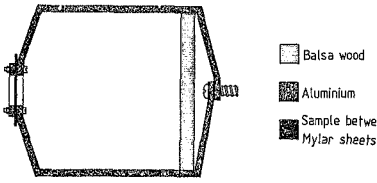


*Fig. 3.3 Frame used to support the absorber in front of the detector.*

The Michelson interferometer (Cosgrove et al. (1971)) provided a means for accurately determining the drive velocity. Whenever the drive moved a distance $\lambda/2$ (where $\lambda$ is the wavelength of the laser light), a light and a dark fringe pass a photodetector. These fringes are counted by the MCA. If each channel is open for the dwell time $\tau$ then the velocity $v$ corresponding to channel $X$ is

$$v_X = N_X \lambda / 2P\tau \qquad (3.2)$$

where $P$ is the number of times the MCA scanned through the channels ($N_X/P$ is thus the "counts per pass"). The average velocity associated with each channel is accurately determined. An example of a calibration spectrum is shown in figure 3.4. Notice that where the velocity is zero, the number of fringes is not. This can be explained as follows:

Suppose there is a distribution of velocities about the mean velocity in channel $X$. For a particular pass ($i$) and channel $X$,

$$v_i = v + \delta v_i \qquad (3.3)$$

where $v$ is the average velocity and $\delta v_i$ is the deviation from the average for that pass. The number of fringes counted in channel $X$ is related to the absolute value of the velocity as follows

$$N=(2\tau P/\lambda)<|v+\delta v_i|> \qquad (3.4)$$

where <> denotes the average. The order in which the average and absolute value is taken may be reversed provided the argument always has the same sign. In this case the average may be taken first if $v-\delta v_i > 0$ for all $i$, so $N=(2\tau P/\lambda)v$, because $<\delta v_i>=0$. But if the velocity is zero, then the number of counts is related to the deviation of the velocity from the mean, i.e. $<|\delta v_i|>$ which is not equal to zero. One could even extract the distribution of velocities about $v=0$ by extrapolating the mean velocity from higher velocities and subtracting this from the region close to $v=0$. In practice this is not so simple since the count also seems to depend on irregularities in the mirrors of the interferometer as well as on the velocity distribution.

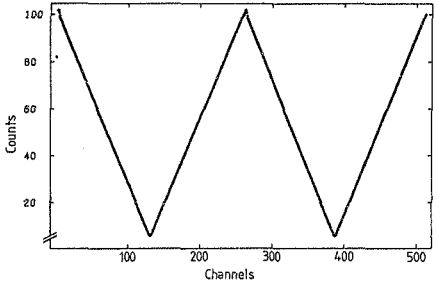


*Fig. 3.4 A velocity calibration spectrum. There are two triangles because the number of fringes counted is related to |v|, so the sign of the velocity must be independently determined.*

Oven and Temperature Controller

To perform Mössbauer investigations at high temperatures, an oven was designed and built. The requirements of such an oven are stringent, particularly if studies near a critical point are contemplated. The temperature stability must be extremely good. Also, a particular problem associated with the Mössbauer effect is that the oven must be transparent to the "soft" $\gamma$ rays associated with many Mössbauer isotopes. In addition, our oven was required to fit between the poles of an electromagnet and to be constructed of materials that would not

distort the magnetic field. Note in figure 3.5 the inner/outer oven arrangement for improved temperature control and stabilisation, and the special windows in the path of the γ rays.

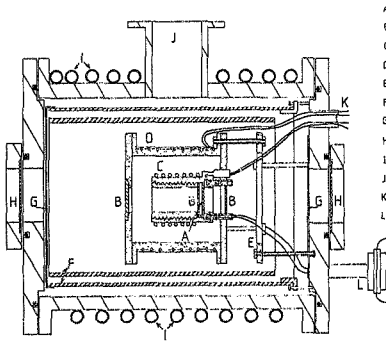


*Fig. 3.5 A cross section of the Mössbauer oven.*

The stainless steel heat shields and efficient evacuation of the oven means that only 168W yields a temperature of 1000K; 158W of this power is dissipated in the outer oven and only 10W in the inner oven. The vacuum is maintained by a diffusion pump with a liquid nitrogen ($LN_2$) trap. The pressure at the top of the $LN_2$ trap is $10^{-7}$torr. In addition to providing a better vacuum, the trap prevents contamination of the sample in the oven by backstreaming of diffusion pump oil. In order to keep the trap full of $LN_2$, a timer/filler was designed and built (see Appendix A).

The oven as illustrated in figure 3.5 was found to have a temperature stability of about 0.5K at 1000K with normal variations in ambient temperature. This however, is not sufficient for experiments near the Curie temperature. Therefore a temperature controller was designed and built, utilising locally available components, as illustrated in figure 3.6.

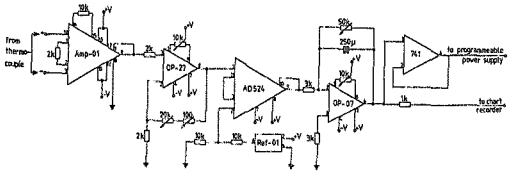


*Fig. 3.6 Schematic diagram of the temperature controller circuit.*

The input to the temperature feedback controller was obtained from one of two Cromel-Alumel thermocouples. (The other was used to measure the temperature.) The thermocouple voltage to the first amplifier stage is amplified 100 times. The critical component of this stage is the precision instrumentation amplifier AMP01. The output voltage is a few volts, which is no longer sensitive to extraneous thermal emf's and temperature drifts. The signal is then passed to the input of the control part of the circuit. The gain of the next amplification stage determines the temperature set point. After the set point amplifier, the signal is

compared with a constant five volt reference using another precision instrumentation amplifier (AD522). Any difference between the five volt reference and the signal derived from the thermocouple is amplified with a gain of 1000. Finally, before the output is used to drive a programmable power supply, the signal is passed through an integrator with a time constant of a few seconds. The gain of the integrator stage is variable and is used to vary the sensitivity of the output to a change in the input. The programmable power supply then changes the current through the inner oven heater in response to the output from the controller. The performance of the oven and controller was good enough for reliable spectra to be acquired within 0.03K of the Curie temperature.

The thermocouples were calibrated relative to the Curie temperature of iron before and after each series of measurements because the thermocouple was reproducible only within two or three degrees. This drift in thermocouple reading has many origins. Firstly, when the thermocouple is installed, bending and twisting the wires induces crystal defects which change the electrical characteristics slightly. With the oven kept at high temperatures for long periods, these (and other) thermally unstable defects are annealed, sometimes to the extent that a single grain boundary can occupy the entire cross section of the wire with consequent change in emf. The wire is also likely to break at such a grain boundary. In addition, such high temperatures facilitate diffusion of atoms out of or into the wires.

The variation of the line width with temperature within about 0.5K of the transition was used to calibrate the thermocouple. A line is fitted to the widths below the transition temperature. The temperature at which this line intersects the average width of single line spectra taken at temperatures far above the transition is defined as the Curie tem-

perature (see figure 3.7). This temperature could be determined to better than 0.1K for all the experiments performed.

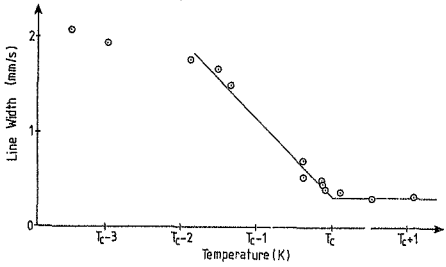


*Fig. 3.7 The variation of the line width as a function of temperature at the Curie temperature.*

The temperature gradient is less than 0.03K across the sample because otherwise it would have been detected as a line broadening in the Mössbauer spectra taken close to the Curie temperature. The applied magnetic field also has an influence on the thermocouple voltage. By turning the magnetic field on and off and observing the thermocouple voltage, it was found that the voltage changed by 33μV/T, which corresponds to a temperature correction of 0.165K with an applied field of 2kG.

## The magnet

The 18cm diameter pole pieces of the Newport Instruments electromagnet were 15cm apart, allowing the oven to fit snugly and ensuring that the field was homogeneous to within 1% across the sample.

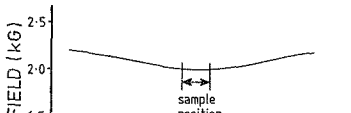


*Fig. 3.8 The variation of the applied magnetic field as the probe is moved from the South pole to the North pole of the magnet. An NMR gaussmeter was used.*

Although the water-cooled coils are rated for drawing 20Amps, the magnet coils became hot (60°C) at a current of 7A per coil. This provided a field of 0.2T at the sample. Figure 3.8 shows the spatial variation of the magnetic field between the pole faces. The field remained constant in time (to within 1%) after the magnet coils had had sufficient time to warm up (about 1 hour).

Before sensible comparisons could be made between spectra taken with and without the magnetic field at high temperatures, room temperature spectra were recorded with and without the applied field. The field could have affected the proportional counter which relies on the ions moving from the cathode to the anode in a straight line and the source line width by inducing a small hyperfine field in the source. To minimise these effects the source and detector were both enclosed in μ-metal sheet except for an aperture for the γ rays. The cooling water through the coils could have caused additional broadening due to vibrations. The comparison of these room temperature spectra showed that all these effects were negligible.

## Overview of the facility

The spectrometer consisting of the laser interferometer, drive and oven is positioned on a track for easy alignment. The track is mounted on shock absorbing rubber grommets, which in turn are mounted on a trolley for easy removal from the magnet. The spectrometer is shown in figure 3.9.

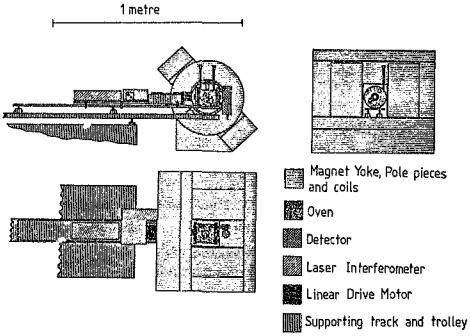


*Fig. 3.9 The spectrometer illustrated to scale.*

## DATA ANALYSIS

### Fitting the data

First the data had to be transferred to the IBM/370 mainframe computer. This was achieved in two stages. A simple circuit for translating current loop logic into EIA standard RS-232-C was constructed (see Appendix A). This allowed the Rainbow PC100 microcomputer to read in the data file using the CP/M-86/80 operating system utility programs. The spectrum was stored on floppy disk. The Rainbow PC100 was then attached to the mainframe via a modem and the data was transferred using the POLY-XFR/TRM terminal emulation package.

Two types of data were analysed: calibration data and spectra. The calibration data were analysed using the program LASERCAL developed at Boston University and adapted to the Wits IBM/370 mainframe. This performed a linear regression on each of the four quarters of the spectrum and produced as output the velocity per channel in each quarter and the two positions of zero velocity (in channels). This output was then used as input to the program used to fit the spectra. The procedure of taking a calibration spectrum before and after each measurement enables us to obtain accurate results for the hyperfine parameters.

The spectra were analysed using a modified version of the program MOSFUN (Müller (1980)). This program uses a non-linear least squares method (either Newton's method or the gradient method) to fit correlated Lorentzian peaks to the data. If $F(v)$ is the theoretical function

describing a spectrum containing $M$ lines, then the form of $F(v)$ used was,

$$F(v)=g(v)\{B-\sum_{m=1}^{M} I_m[1+(v-v_m/\Gamma_m)^2]^{-1}\} \qquad (4.1)$$

where $g(v)$ is the so-called geometric factor, $B$ is the baseline of the spectrum and $I_m$, $v_m$ and $\Gamma_m$ are the intensity, position and half the full width at half maximum for line $m$, respectively. The geometric factor modulates the baseline radiation; as the source moves away from the absorber, the solid angle, subtended by the sensitive area of the detector at the source, decreases as does the observed count rate. Similarly, as the source moves closer to the detector, the count rate increases.

If no absorber were present,

$$g(v)=F(v)/B \qquad (4.2)$$

Clearly, $F(v)\propto(r(v))^{-2}$ and $B\propto(r_s)^{-2}$ where $r(v) = r_s + \Delta r(v)$ is the distance from the absorber to the detector expressed as a function of velocity, $r_s$ is the mean of $r(v)$, and $\Delta r(v)$ the displacement of the source relative to its mean position. Now,

$$g(v)=(1+(\Delta r(v)/r_s))^{-2} \qquad (4.3)$$

Since $\Delta r(v)$ is a quadratic function of $v$ (displacement is the integral of the velocity, and the velocity changes linearly with time) which can be determined to within a constant factor, only one fit parameter is required for the geometric effect.

For a simple single line spectrum, the Lorentzian parameters--intensity, position and width--are simply fitted using equation 4.1. For six line magnetically split spectra, to fit the lines independently would require 18 parameters for the peaks alone. However, the positions of the six absorption lines are given by

$$\nu(m_e, m_g) = \delta + \mu_g H[(m_g/j_g) - (m_e\mu_e/j_e\mu_g)](\frac{c}{E_0}) \qquad (4.4)$$

where $\delta$ is the isomer shift and the second term follows from equation 2.21. The quantities associated with the nuclear ground and excited states are denoted by the subscripts $g$ and $e$, respectively. The energy has been converted to velocity using the first order Doppler shift equation 3.1. Equation 4.4 tells us that the splitting of the lines may be characterised by only one parameter, the hyperfine field. The positions of each of the six lines with respect to the centre of the spectrum can then be calculated by multiplying the hyperfine field by the constant factor associated with each line. The position of the centre of the spectrum with respect to zero velocity requires an additional parameter, the isomer shift $\delta$. In addition, in most cases both lines in the pairs 1 & 6, 2 & 5 and 3 & 4 should have the same intensity, i.e. only three intensity parameters are required. To a good approximation, the widths of all six lines are also the same. One therefore needs only six parameters to describe a magnetically split iron spectrum. The association of the parameters with the lines in the correct way is achieved using a correlation matrix in the program MOSFUN.

It was necessary to modify and extend this program so that all the relevant information from LASERCAL could be used. MOSFUN used only three parameters to describe the triangular velocity scale. These were the maximum velocity, the period (in channels), and the folding point. This ignores possible effects such as a small non-linearity in the ve-

locity variation or more importantly, an asymmetry in the velocity triangle. The routine was rewritten to use six parameters, viz. the velocity increase per channel in each of the four quadrants and the two positions of zero velocity (in channels). This change in velocity calibration also necessitated a change in the calculation of the geometric factor, since this was calculated in a way which relied on the convenient symmetrical form in which the velocity had been expressed. By reading in the dwell time as an additional parameter, the displacement of the moving source is calculated explicitly by integrating the velocity and assuming the source is in its equilibrium position when the velocity is at its maximum. The geometric fit parameter is now simply the ratio of the maximum deviation of the source from its equilibrium position, to the mean distance from the source to the detector. This quantity can be readily verified in the experimental setup.

MOSFUN expresses all parameters in units of velocity. Both halves of a spectrum could be accurately fitted simultaneously without folding. Effectively this doubles the number of absorption lines that have to be accounted for by the fit, and improves the reliability of the parameters obtained from the fit. Moreover, to determine the absorption area, the baseline and background counts must be accurately known. The baseline can usually be well determined if the spectrum is fitted with Lorentzian peaks, and the potentially large error incurred by neglecting the tails of the Lorentzian peak becomes smaller. However, if only one half is fitted at a time, the least squares technique may distort the baseline (or geometric correction) in order to improve the fit. This can lead to serious errors in the measured areas. By fitting both halves simultaneously with an accurate calibration of the velocity, this freedom is denied the fitting procedure.

## Determination of hyperfine parameters

The hyperfine parameters measured are the magnetic hyperfine field, the isomer shift, the line widths, the intensity ratios and the absorption area.

These could all be extracted from the output from MOSFUN. Factors which improved the accuracy and precision of the above numbers are: the total count, the background, how well the peaks were resolved, and the accuracy of the velocity calibration. Where possible, the total count exceeded $10^5$ per channel, and the background was kept as low as possible. For measurements without the oven, the background was less than 10%. With the oven, a background of up to 40% was tolerated.

# THE RECOILLESS FRACTION OF IRON CLOSE TO THE CURIE TEMPERATURE

First the absorption area method commonly used for evaluating the recoilless fraction of absorbers is discussed. Next, two methods for determining the recoilless fraction of sources are presented. Because of anomalies in the absorption area at the Curie temperature due to saturation effects, we cannot apply the absorption area method to evaluate the recoilless fraction of an iron absorber. To avoid these saturation effects, we measured the recoilless fraction of a $^{57}Co(^{56}Fe)$ source.

## Determining the recoilless fraction of an absorber

The probability $\varepsilon(v)$ that a photon from a source is absorbed at a velocity $v$ is related to the number of counts $N(v)$ detected at that velocity through

$$N(v) = N(\infty)-\varepsilon(v)N_\gamma \qquad (5.1)$$

where $N(\infty)$ is the count at infinite velocity (often taken to be the baseline count at the largest velocity in the spectrum) and $N_\gamma$ is the number of $\gamma$ rays of the Mössbauer transition.

The probability $\epsilon(\nu)$ can be written as the product of the probability $f_s$ that a recoilless $\gamma$ ray is emitted from the source and a convolution of the emission line shape $L(E;E_\nu,\Gamma_s)$ with the probability of resonant absorption of a $\gamma$ ray with a particular energy $E$.

$$\epsilon(\nu) = f_s \int_{-\infty}^{\infty} L(E;E_\nu,\Gamma_n)\ \{1-e^{[-n_a \sigma(E;E_s',\Gamma_n)]}\}\,dE \qquad (5.2)$$

where $L(E;E_\nu,\Gamma_n)$ is the ubiquitous Lorentzian distribution

$$L(E;E_\nu,\Gamma_n) = \frac{2/\pi\Gamma_n}{1+[2(E-E_\nu)/\Gamma_n]^2} \qquad (5.3)$$

$\Gamma_n=\hbar/\tau$ is the natural line width of the nuclear transition, $E_\nu=E_s(1+\nu/c)$ is the centre of the Lorentzian distribution of the source which has been Doppler shifted because of its motion, $E_s$ and $E_s'$ are the nuclear transition energies in the source and absorber respectively, $n_a$ is the number of absorber nuclei per unit area in the absorber, and $\sigma(E;E_s',\Gamma_a)$ is the resonant absorption cross section, which also has a Lorentzian shape and includes the recoilless fraction $f_a$ of the absorber as a factor.

$$\sigma(E;E_s',\Gamma_a) = \frac{f_a \sigma_0}{1+[2(E-E_s')/\Gamma_a]^2} \qquad (5.4)$$

$\sigma_0$ is the maximum absorption cross section and $\Gamma_a$ is the line width of the nuclear transition in the absorber (often $\Gamma_a=\Gamma_n$ ).

The area (in dimensionless units) of the absorption spectrum is usefully written as

$$A = (2/\Gamma_m) \sum_m \frac{N(\infty) - N(m)}{N(\infty) - N_B} = \frac{2}{\Gamma_m} \int_{-\infty}^{\infty} \varepsilon(v)dv \qquad (5.5)$$

The sum runs over the $m$ channels and $\Gamma_m$ is the minimum observable line width measured in velocity units, i.e. $\Gamma_m = 2\Gamma_n c/E_\gamma$. Inserting the expression for $\varepsilon(v)$ and changing the order of integration, one obtains

$$A = f_s \frac{1}{\Gamma_n} \int [1 - exp[-n_a \sigma(E;E_\gamma',\Gamma_a')]]dE \qquad (5.6)$$

The area is a function of the dimensionless quantity

$$t_a = n_a f_a \sigma_0 \qquad (5.7)$$

which enters in the exponent under the integral in equation 5.6 as can be seen if equation 5.4 is inserted in equation 5.6. The quantity $t_a$ is a measure of the effective absorption thickness of the absorber for recoilless $\gamma$ rays.

The $f_a$ value can be evaluated from equation 5.6 provided that $A$ and $f_s$ are accurately known, using a special program written by D.B. Hall (1984). A major error in absorption area measurements is the uncertainty in the baseline count $N(\infty)$. By fitting both halves simultaneously, as described in chapter 4, the freedom to distort the baseline for obtaining a better fit is denied the fitting procedure, improving the accuracy of our areas.

Although the expression 5.6 was derived for a Lorentzian $\gamma$-ray distribution for the source, it relies only on the fact that the integral over velocity of the source distribution is unity. Any vibration of the absorber can be equivalently thought of as vibrations of the source and so will not change the absorption area. This means that the absorption area method is not influenced by instrumental broadening. It

will, however, be affected by a splitting or broadening through hyperfine interactions in the absorber due to the so-called saturation effects. For $t_a \ll 1$ , the absorption area is linear in $t_a$ , whereas for $t_a > 1$ the absorption area starts to saturate (figure 5.1). To illustrate this effect on the absorption area, the area of a single line is compared with that of a doublet in figure 5.1. The effective thickness $t_a$ for both absorbers is assumed to be the same. Clearly the sum of the two areas for the doublet is greater than the area of the single line. Since the absorption spectrum of iron splits into six lines at the Curie temperature, this is expected to have a large impact on the absorption area. Even without any change in the recoilless fraction, a jump in the absorption area of an absorber is expected at the Curie temperature. From such a jump it is difficult to extract small changes in the recoilless fraction.

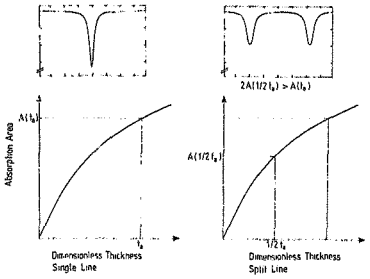


*Fig. 5.1 Illustration of the change in area as a line splits. (The absorber has the same recoilless fraction and the same total number of absorber nuclei in both cases.)*

## Determining the recoilless fraction of a source

To avoid the saturation effects in an absorber described in the previous section, recoilless fraction measurements can be performed on a source. The recoilless fraction of a source can be determined in two ways. The simplest method, provided that the source emits a single line, is the elegant Black absorber technique developed by Housely et al. (1964). The Mössbauer spectrum of the black absorber is illustrated in figure 5.2. This absorber consists of a mixture of ammonium-lithium fluoroferrate.

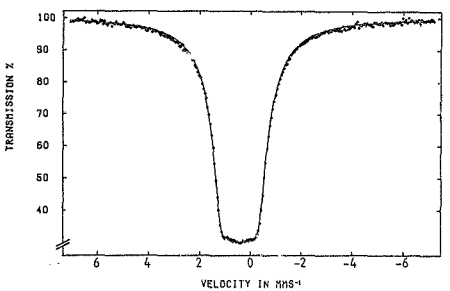


*Fig. 5.2 The spectrum of a black absorber recorded with a $^{57}Co(Rh)$ source.*

Almost complete absorption of recoillessly emitted γ rays is achieved over a velocity range of about 1mm/s. Schematically, the experiment is set up as in figure 5.3. If the absorber is stationary and the isomer shift of the source is not too large, then practically no resonant γ rays

can be detected. If however, the black absorber is vibrated so the velocity is less than 1mm/s for less than, say, 1% of the time, then 99% of the recoilless $\gamma$ rays will be detected. From the counts with the black absorber stationary $N(0)$ and the counts with the absorber vibrating $N(\infty)$ corrected for the background $N_B$, a good estimate of the recoilless fraction can be obtained using

$$f_{est} = \frac{N(\infty) - N(0)}{N(\infty) - N_B} \qquad (5.8)$$

This estimate can be improved by taking into account various corrections as discussed in Kolk (1981).

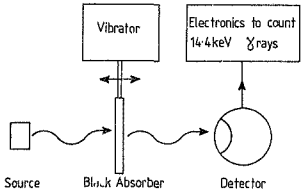


*Fig. 5.3 The experimental arrangement for the black absorber method.*

When the source emission line splits, the black absorber technique cannot be applied, so the absorption area method has to be used with an absorber at constant temperature. From equation 5.6 one can derive,

$$f_s(T) = A(T) f_0 / A_0 \qquad (5.9)$$

where $A_0$ is the absorption area of the absorber taken with a source of known recoilless fraction $f_0$, and $A(T)$ is the absorption area obtained with the source of interest.

Determining the background radiation

All the above methods for determining the recoilless fraction depend on a reliable estimate of the background. The background radiation comes predominantly from $\gamma$ rays of higher energy than 14.41keV which have lost some energy so that they are detected as 14.41keV $\gamma$ rays. These counts must be subtracted from the spectrum before the recoilless fraction can be determined. Any inaccuracy in the determination of the background will obviously affect the results.

The background was determined using the standard procedure of measuring the count rate with and without a copper foil. The ratio of these two counts is a rough estimate of the background if a foil of suitable thickness is used, so almost all the 14.41keV $\gamma$ rays and almost none of the 122keV and 136keV $\gamma$ rays are absorbed. The foil we used has a mass per unit area of 0.080g/cm$^2$. Corrections for the 122keV and 136keV $^{57}$Fe $\gamma$ rays absorbed by the foil and 14.4keV Mössbauer $\gamma$ rays transmitted by the foil are relatively small. The correction for the 23keV X-rays from Rh atoms is not as simple because of the proximity in energy to 14.41keV. For our measurements, the background was corrected using a range of substantially thinner copper

foils as well as a much thicker foil. Assuming that the mass absorption coefficients for copper at the different energies are known, the contribution from the higher energy $\gamma$ rays can be isolated with the thick foil The thinner foils then permit the contribution of the 23keV $\gamma$ rays to be differentiated from that of the 14.41 $\gamma$ rays because the different mass absorption coefficients for the two energies is sufficiently different. The background had to be increased by 20% in our case because the width of the discriminator window was set too large. Even if the discriminator window is set optimally for a proportional counter the correction is still substantial ($\simeq$ 5%). It should be noted that no reference to such a correction could be found in the literature. Apparently in previous recoilless fraction measurements reported in the literature, this fairly substantial correction has not been taken into account. To ensure that the background was accurately determined, it was measured every eight hours during the measurement. A weighted average of these measurements was used.

The recoilless fraction of an iron source

The source measurements were performed on a custom-made source of $^{57}$Co in a matrix of 100% enriched $^{56}$Fe. The absence of $^{57}$Fe means that there is no self-absorption. Although corrections can be made, self-absorption will show similar saturation effects to those present in an iron absorber. Above the Curie temperature, the $^{57}$Co($^{56}$Fe) source emits only one recoilless $\gamma$-ray line, and the black absorber technique can be applied (see equation 5.8). However, the isomer shift between the $^{57}$Co($^{56}$Fe) source and the black absorber is rather large. The peak of the source $\gamma$-ray line lies at the edge of the black absorption

region, requiring substantial corrections. Kolk and Hall (1983) measured the recoilless fraction of the source above the Curie temperature using this technique. Their measurements are plotted in figure 5 4.

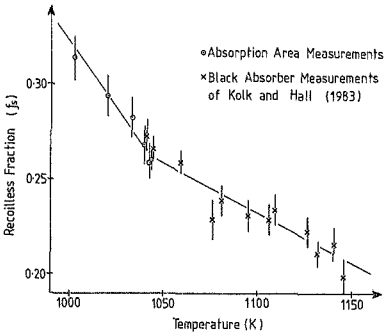


*Fig. 5.4 The recoilless fraction of $^{57}Fe^{*}$ in iron consisting of 100% enriched $^{56}Fe$ close to $T_C$. (* indicates the excited state.)*

Also of interest is the recoilless fraction of the source just below the Curie temperature. The black absorber method then no longer applies and we have to resort to the absorption area method (see equation 5.9).

Seven spectra were acquired at temperatures from 40K below the Curie temperature to the Curie temperature. The source was placed in the oven and the room temperature absorber used was a 25μ stainless steel foil. Because of the low source activity, each measurement took about 15 days to accumulate sufficient counts ($10^5$ counts per channel). Spectra recorded in this temperature region are shown in figure 5.5.

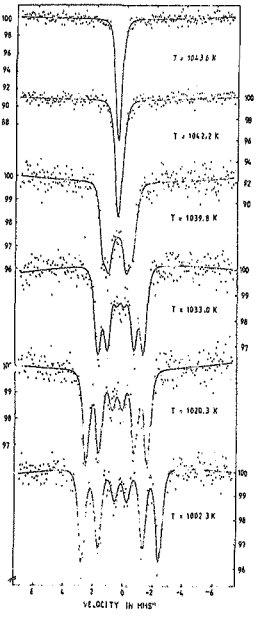


*Fig. 5.5 Spectra with a stainless steel absorber and $^{57}Co(^{\nu}Fe)$ source close to the Curie temperature.*

The single Mössbauer absorption line of the stainless steel absorber is broadened by relaxation phenomena. The spectra were therefore fitted with an approximation to a Voigt line which is a convolution of a Gaussian and a Lorentzian peak. All the spectra recorded with this absorber were fitted with the same proportion of Lorentzian and Gaussian characters. This was necessary because a Lorentzian has bigger "tails" than a Gaussian. The line width obtained was 0.45mm/s. The reference absorption area $A_0$ in equation 5.9 was measured with a $^{57}$Co(Rh) source. The recoilless fraction of this source $f_0 = 0.713 \pm 0.005$ was determined by the black absorber method. The recoilless fraction values calculated from these spectra are plotted in figure 5.4.

The recoilless fraction of an iron absorber

Thirty spectra were acquired using a natural iron absorber in the vicinity of the Curie temperature of iron. The areas of the spectra are plotted in figure 5.6. There is a marked increase in the area at the Curie temperature due to the saturation effects illustrated in figure 5.1. The area as a function of temperature was calculated from equation 5.6 using a program written by D.B. Hall (1984). This program requires the hyperfine field and line width of the absorber and the recoilless fraction of the source as input. If one assumes that the absorber has the natural line width, then the best fit is obtained with recoilless fraction values for the absorber which are 30% larger than the values obtained using the black absorber method for the source. However, if one assumes that the absorber exhibits a small line broadening of 0.005mm/s (5%) then the $f_a$ values required to fit the area data are reduced by 25%. Hall's program was modified to use as input the recoilless fractions from figure 5.4. The solid curves in figure 5.6 show the area was calculated for three different absorber line widths $\Gamma_a$. Clearly, $1.031 < (\Gamma_a/\Gamma_n) < 1.134$. The best fit was obtained

with $(\Gamma_a/\Gamma_n) = 1.15$ . It must be emphasised that this line broadening cannot be caused by instrumental broadening because the area is not affected by such broadening as pointed out after equation 5.7.

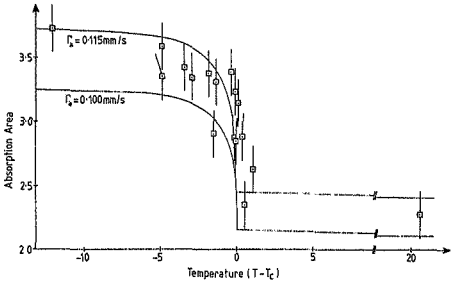


*Fig. 5.6 Absorption area of a 25μ natural iron foil recorded with a $^{57}Co(Rh)$ source at temperatures near the Curie point.*

# THE HYPERFINE FIELD OF IRON NEAR THE CURIE POINT

## The relation between hyperfine field and magnetisation

The hyperfine field is an effective way of studying the magnetic properties of iron. In chapter 2 it was stated that the dominant contribution to the hyperfine field arises from the Fermi contact interaction given in equation 2.23. This interaction measures the net $s$ electron spin at the nuclear site caused by the net moment of the $d$ electrons through core polarisation. For this chapter, we assume that the Fermi contact interaction is the only contribution to the hyperfine field.

The nucleus samples the hyperfine field on a time scale determined by the Larmor period of the nucleus in that hyperfine field, given by

$$\tau_L = 2\pi \frac{\hbar j}{\mu H} \qquad (6.1)$$

where $H$ is the hyperfine field, $\mu$ is the nuclear magnetic dipole moment and $j$ is the nuclear spin. In the limit where the hyperfine field fluctuates with a period $\tau_R \ll \tau_L$, the nucleus experiences a time average of the hyperfine field, which is proportional to the average moment of the $d$ electrons. The average moment per unit volume is defined as the magnetisation, and so

$$H(T)/H(0) = M(T)/M(0) \qquad (6.2)$$

One does not expect this relationship to remain valid as the rate of relaxation slows down.

Measurements above the Curie temperature in an applied field.

Measurements were performed in an applied magnetic field at a temperature 0.75K above the Curie temperature ($T_C$). These measurements are shown in figure 6.1. The hyperfine field was determined from fitting the spectrum with Lorentzian lines according to the method in chapter 3. For spectra with a hyperfine field of less than 3T the hyperfine field is not well determined because the line width and hyperfine field are strongly correlated, i.e. a reduction in the hyperfine field can be compensated by increasing the width and adjusting the intensities slightly to achieve an equally good fit to the data.

The spectra display anomalous behaviour of the line intensity ratios. According to equation 2.25 the ratio of the six lines in the Mössbauer spectrum of a nonmagnetised iron foil are given by

3:2:1:1:2:3,

and for a foil magnetised perpendicular to the direction of the $\gamma$-ray propagation by

3:4:1:1:4:3.

In our measurements the iron foil is magnetised perpendicular to the $\gamma$-ray beam by the externally applied field. At sufficiently high external fields (.2T) the foil is fully magnetised, and one expects the ratio of lines 1 and 6 to lines 2 and 5 to be 3:4. This is in agreement with the measured line intensity ratios displayed in Fig. 6.2. However, when the external field is decreased one expects this ratio to increase to 3:2, whereas the measured ratios show a decrease, i.e. just the opposite effect. This anomaly cannot be explained by saturation effects because these effects would increase instead of decrease the ratio.

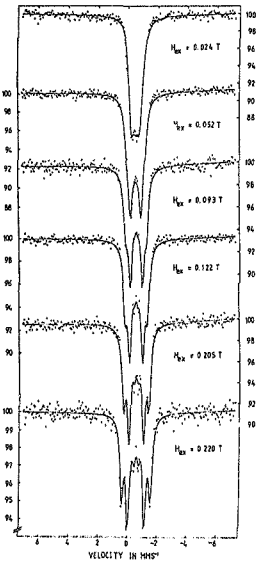


*Fig. 6.1 Spectra of iron in various applied fields 0.7K above the Curie temperature.*

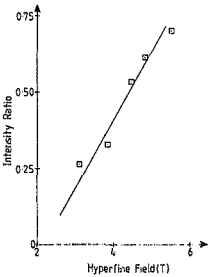


*Fig. 6.2 Ratios of the line intensities as a function of applied field at 0.75K above the Curie temperature.*

Figure 6.3 shows the variation of the hyperfine field with the applied field at 0.75K above $T_C$. There is clearly a saturation in the hyperfine field. The saturation value is $H_{sat}$ = 6.4T. One can also calculate the magnetic susceptibility by taking the slope of the line between the origin and the first data point in figure 6.3 using

$$\chi = \frac{M(T)}{H_{applied}} = \frac{H(T)}{H_{applied}} \times \frac{M_0}{H_0} \qquad (6.2)$$

which follows directly from equation 6.1. Taking $H_0$=33T and $M_0$ = 0.17T, one finds $\chi$=*1.32±0.04* . This compares with the value obtained by Noakes et al. (1966) of 1.34 at 0.75K above the Curie temperature. However, our value 1.32 of $\chi$ is a lower estimate because the curve is steeper closer to the origin.

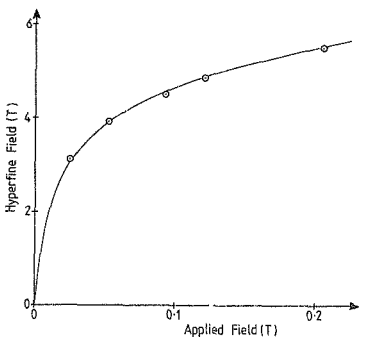


*Fig. 6.3 The hyperfine field as a function of applied field at 0.75K above the Curie temperature.*

On increasing the temperature with an applied field of 0.2T, the hyperfine field decreased as shown in figure 6.4, tending to zero at 20K above the Curie temperature. Again a saturation was observed, this time as the temperature approached the Curie temperature. The saturation value obtained in this series of measurements is $H_{sat}$ =6.5T. Data for an applied field of 0.1T are also shown in figure 6.4.

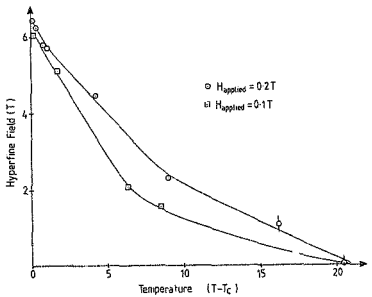


*Fig. 6.4. Hyperfine fields of iron induced by applied fields of 0.1T and 0.2T for temperatures above $T_C$. The lines shown are drawn by hand to guide the eye.*

When an external field was applied at temperatures below the Curie temperature, an increase in the hyperfine field was observed. Figure 6.5 shows yet again a saturation at $H_{sat}$ =6.3T. The average of the three saturation hyperfine fields above is $\langle H_{sat} \rangle$ =6.4±0.2T. Since a hyperfine field of 33T is produced by a magnetisation of $2.2\mu_B$ (Bohr magnetons) per iron atom in iron at room temperature, the average magnetisation in iron is $0.43\pm0.02\mu_B$ per atom, within 1K both above and below the Curie temperature.

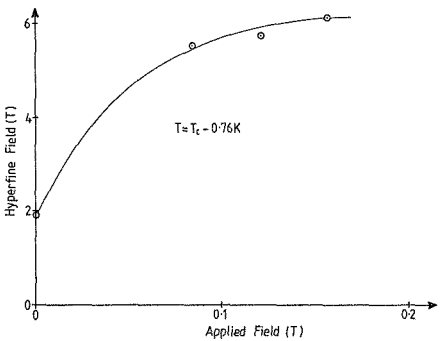


*Fig. 6.5 Hyperfine field of iron at 0.76K below the Curie temperature for various applied fields.*

## DISCUSSION

The recoilless fraction of iron near the Curie temperatu

We established in chapter 5 that the magnetic interaction has a distinct effect on the recoilless fraction. From Fig. 5.4 it follows that the $f$ value of iron changes more rapidly with temperature below the Curie temperature than above it, indicating that the magnetic interaction influences the mean square displacement of the atoms. The recoilless fraction is related to the characteristic temperature $\theta_{-2}^{a}$ (see equation 2.18) by

$$-ln\ f = k^2\langle x^2\rangle = \frac{6E_R T}{k_B(\theta_{-2}^{a})^2} \qquad (5.18)$$

Using this equation, the values of $\theta_{-2}^{a}$ above and below the Curie temperature are determined from the data in figure 5.4. $\theta_{-2}^{a}$ is related to the harmonic characteristic temperature $\theta_{-2}$ by (see equation 2.15)

$$\theta_{-2}^{a} = \theta_{-2}\ [1 - \varepsilon(-2)T] \qquad (5.8)$$

where $\varepsilon(-2)$ is a weighted anharmonic constant. Using $\theta_{-2}$= 439K derived from the phonon spectrum of iron at room temperature (see Johnson, 1970), the values of $\varepsilon(-2)$ below and above $T_C$ can be calculated.

The values for $\theta_{-2}^{a}$ and $\varepsilon(-2)$ are summarised in Table 1.

| | $T<T_C$ | $T>T_C$ |
|---|---|---|
| $\theta_{-2}$[a] | 171 ± 9 K | 241 ± 15K |
| $\varepsilon(-2)$ | $5.8 \pm 0.3 \times 10^{-4}\ K^{-1}$ | $4.3 \pm 0.3 \times 10^{-4}\ K^{-1}$ |

*Table 1*

Hence, our results show that the magnetisation of iron leads to an increase in the anharmonic constant $\varepsilon(-2)$ by

$$\varepsilon(-2)_{T<T_C} - \varepsilon(-2)_{T>T_C} = (1.5 \pm 0.4) \times 10^{-4}\ K^{-1}$$

In addition we found that in the absorber a line broadening of 12% exists. As pointed out in chapter 5, the area method used is insensitive to instrumental broadening. Other possible causes for line broadening are temperature gradients across the sample. In particular, just below $T_C$ small temperature gradients may yield large increases in the line width. However, above $T_C$ a small temperature gradient has hardly any effect on the line width. Temperature gradients cannot therefore explain the observed line broadening because this broadening stretches over a region from 40K below $T_C$ to 100K above $T_C$. Hence, the 12% increase in line width seems to be an effect intrinsic to the absorber. A possible cause may be lattice defects formed at these elevated temperatures.

In only two other recoilless fraction measurements of iron (Preston et al. 1962 and Kovats and Walker 1969), the $f$ value of an iron absorber is evaluated using the absorption area method. In these previous measurements the effect of the magnetisation on the recoilless fraction

was not observed. This is not surprising; because of the large change in the absorption area due to the change in saturation at $T_C$ (see Fig. 5.5), small effects in $f$ are hard to detect. Our $f$ values at room temperature agree with those of Kovats and Walker; at $T_C$ however, our $f$ values are smaller. Comparison of our absorption areas near $T_C$ with those of Kovats and Walker reveal that both areas are practically the same. The reason that Kovats and Walker find a larger $f$ value near $T_C$ is that they have not taken into account the intrinsic broadening observed for the line width of iron near $T_C$.

The hyperfine field of natural iron in an applied field

The average local moment in iron within 1K below and above the Curie temperature was found to be $0.43\pm0.02\mu_B$. This value was deduced from three series of measurements. The first involved increasing the applied field at a fixed temperature 0.75K above the Curie temperature, the second involved decreasing the temperature with a constant applied field of 0.1T and 0.2T to within 0.05K of the Curie temperature, and the third was taken from three spectra at a temperature 0.76K below the Curie temperature whilst varying the applied field.

The initial susceptibility determined from the hyperfine field induced by an applied field was found to be greater than the value of Noakes et al. (1966) from magnetisation measurements. This may be explained by the fact that equation 6.2 derived from relation 6.1 is not valid when the Larmor period of the nucleus is comparable to the fluctuation time of the net magnetic moment. There are strong indications that we are seeing such relaxation effects because of the anomalous intensity ratios

observed in the spectra recorded in small applied fields .75K above the Curie temperature (see Fig. 6.2).

## REFERENCES


Blume, M. and Tjon J.A., (1968) Phys. Rev., 165, 446

*Cosgrove*, J.G. *and* Collins, R.L. (1971) Nucl. Inst. and Meth., 95, 269

Edmonds, A.R. (1974), *Angular Momentum In Quantum Mechanics* (Princeton Univ. Press), *passim*

Hall, D.B. (1983) Masters degree thesis, Boston University

Hall, D.B. (1984) Private communication

Housley, R.M., Erickson, N.E. and Dash, J.G. (1964) Nucl. Instrum. and Meth., 27,29

Hubbard, J. (1978) Phys. Rev. B, 19, 2626

Johnson, D.P.,Phys. Rev. B, 1,3551

Kendall, M.G. and Stuart, A. (1958) *The Advanced Theory of Statistics* (Griffin, London)

Kobeissi, M.A. and Hohenemser, C. (1978) Rev. Sci. Instrum., 49, 601

Kobeissi, M.A. (1981) Phys. Rev. B, 24, 2380

Kolk, B. and Hall, D.B. (1983) private communication

Kolk, B. (1984) in *Dynamical Properties of Solids*, vol. 5, Ed. by G.K. Horton and A.A. Maradudin. (North-Holland, Amsterdam)

Kolk, B., Bieloch, A.L., Hall, D.B., Zheng, Y. and Patton-Hall, K.E. (1985) *accepted for publication* in Nucl. Instrum. and Meth., 27, 29

Kovats, T.A. and Walker, J.C. (1969) Phys. Rev., 181, 610

Maradudin, A.A. (1974) in *Dynamical Properties of Solids*, vol.1, Ed. by G.K. Horton and A.A. Maradudin. (North-Holland, Amst

Mori[illegible] in *Electron Correlation and Magnetism in Narrow Band Sy[illegible]*, by T. Moriya (Springer-Verlag, Berlin)

Müller, E.W. (1980) *MOSFUN, A New and Versatile Mössbauer Fitting Program* (distributed by the Mössbauer Effect Data Center)

Noakes, J.E., Tornberg, N.E. and Arrott, A. (1966) Applied Phys., 37, 1264

Potter, H.H. (1934) Proc. Roy. Soc. (London) A146, 362.

Prange (1981) in *Electron Correlation and Magnetism in Narrow Band Systems*, Ed. by T. Moriya (Springer-Verlag, Berlin)

Preston, R.S., Hanna, S.S. and Heberle, J. (1962) Phys. Rev., 128, 2207

Rose M.E. (1957) *Elementary Theory of Angular Momentum* (Wiley, New York), *passim*

Watson, R.E. and Freeman, A.J. (1961) Phys. Rev. 123, 2027

APPENDIX A

This appendix contains all the electronic circuits designed by the author for the experimental facility. The data sheets of the integrated circuits concerned were consulted when the circuits were designed.

Timer for automatic liquid nitrogen filler

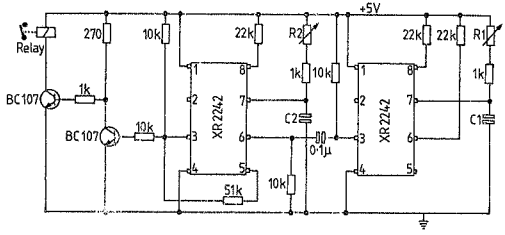


*Fig. A.1 Circuit diagram for liquid nitrogen timer/filler*

This circuit is designed to switch a relay on for a short time (say 1 or 2 minutes) at regular intervals of approximately 4 hours. Both the short and long periods are variable (from 2 seconds to 15 minutes and

from 2 hours to 22 hours respectively). The relay switches a small diaphragm compressor on. This provides overpressure on the dewar so liquid nitrogen is transferred.

The heart of the circuit is the XR2242 long-range timer I.C. Two of these I.C.'s are cascaded in order to produce at the output of the second a signal that is 5V to turn the relay off and 0V to turn the relay on. The period of each timer in seconds is 256RC where the resistance R and the capacitance C are connected to pin 7 of the I.C. $R_1$ consists of eleven 100kΩ resistors in series so that the resistance can be switched from 0kΩ to 1.1MΩ in 100kΩ steps. $C_1$ is 277μF which gives a maximum time of 21.7 hours decreasing in 2-hour intervals to a few minutes. A 1kΩ resistor was connected in series with $R_1$ so that the resistance was not zero. $R_2$ and $C_2$ were similarly chosen to give a maximum time of 18 minutes.

The two timers are coupled by $C_3$. Timer 1 produces a square wave with a period $256R_1C_1$ seconds at pin 3. When the output of timer 1 changes to 5V a pulse is produced at the trigger of timer 2 (pin 6). When the output of timer 2 changes to 5V, timer 2 resets itself via $R_3$ (connected to pin 5). Timer 2 remains in the reset state until it is triggered again by timer 1. When the output of timer 2 is 0V, the relay is energised by the inverting network of transistors 1 and 2.

MCA pass counter circuit

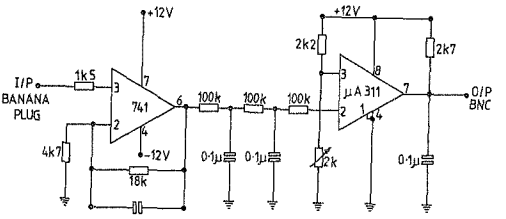


*Fig. A.2 Circuit diagram of pass counter.*

Most MCA's store the number of passes, either in channel 0 or in a separate memory. Although the number stored in channel 0 of the Nuclear Data MCA used in these experiments did not contain data, we were unable to relate this number to either the time or the number of passes. The following circuit was designed to count the number of passes on a conventional NIM module counter using the signal which controls the time base of the MCA display oscilloscope. The circuit consists of a three-stage low pass filter and a comparator. The low pass filter was necessary because the signal had large voltage spikes superimposed on the ramp.

Circuit for converting current loop to RS-232-C compatible signal

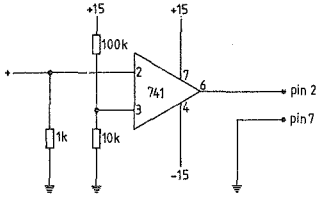


*Fig. A.3 20mA current loop to RS-232-C signal converter.*

The output of the Nuclear Data MCA was a 110 baud current loop teletype signal. To enable the DEC Rainbow PC100 microcomputer and the DEC MICRO-PDP-11 computer to read and store the data, the signal had to be converted to the RS-232-C standard. The current loop sends a current of 20mA when the data logic is high and no current when it is low. Conversely, the RS-232-C signal is less than -5V when the data logic is high (1) and more than +5V when it is low (0). This conversion was simply accomplished using a 741 operational amplifier in the circuit in figure A3.

## ACKNOWLEDGEMENTS

Working to a tight deadline is always difficult, probably this thesis has been no exception. *I would like to express my sincere thanks* to the following people who helped make this work possible. Prof. Berend Kolk who has given me an introduction to experimental physics that will last a lifetime. My family for their unfailing support, greater than anyone could have wished for. I would like especially to thank my sisters Roz and Helen for committi themselves to the last minute frenzy. Di Franz for all the diagrams and hours spent in the lab with me. Tony Albers and Gio Hearne, more stimulating and helpful fellow *students do not exist*. Dr. P.T. Wedepohl of MINTEK for organising financial assistance and for his friendly support. Prof. A.M. Starfield who never fails to take a keen interest in my endeavours. Lastly the members of the University of the Witwatersrand Physics Department. In writing these acknowledgements, I know how meagrely they repay those who have helped me so unselfishly.

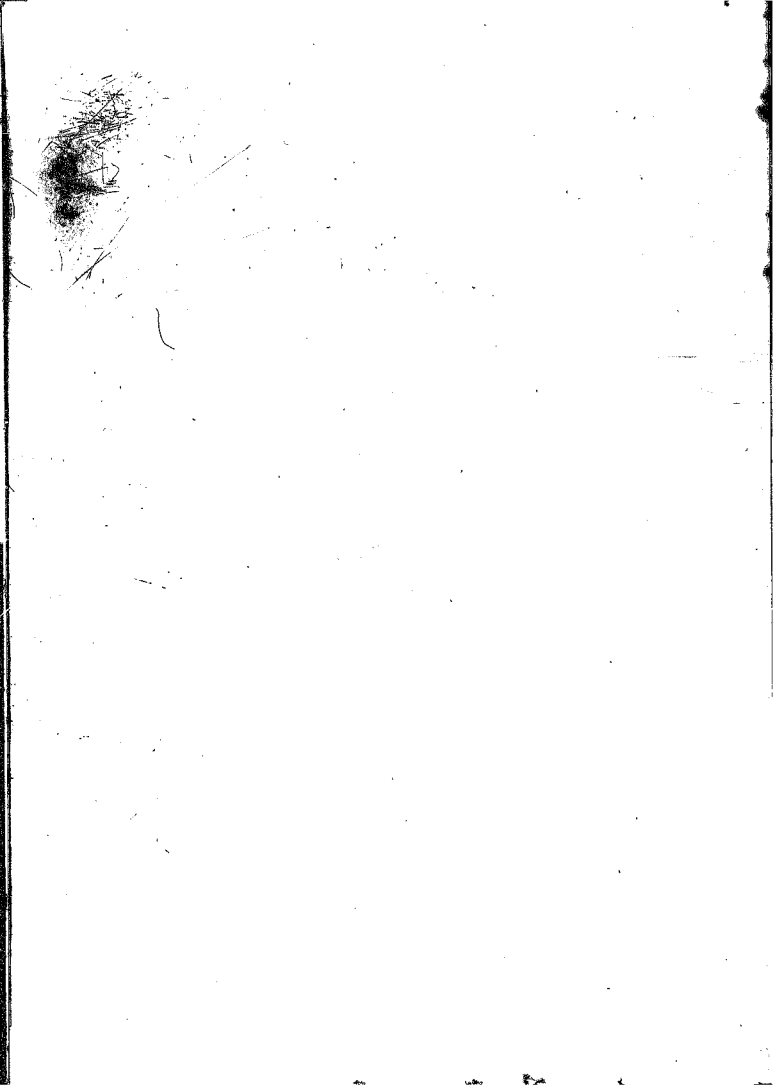

**Author** Bleloch Andrew Luke
**Name of thesis** Mossbauer Effect Spectroscopy Of Iron Near The Curie Temperature. 1985

*PUBLISHER:*
**University of the Witwatersrand, Johannesburg**
**©2013**

*LEGAL NOTICES:*

**Copyright Notice:** All materials on the University of the Witwatersrand, Johannesburg Library website are protected by South African copyright law and may not be distributed, transmitted, displayed, or otherwise published in any format, without the prior written permission of the copyright owner.

**Disclaimer and Terms of Use:** Provided that you maintain all copyright and other notices contained therein, you may download material (one machine readable copy and one print copy per page) for your personal and/or educational non-commercial use only.

The University of the Witwatersrand, Johannesburg, is not responsible for any errors or omissions and excludes any and all liability for any errors in or omissions from the information on the Library website.